Reproducibility of the GIS Non X-Ray Background

Y. Ishisaki[1], Y. Ueda[2], H. Kubo[2], Y. Ikebe[3], K. Makishima[4] and the GIS team

[1] Department of Physics, Tokyo Metropolitan University
[2] Institute of Space and Astronautical Science
[3] Institude of Physical and Chemical Research (RIKEN)
[4] Department of Physics, the University of Tokyo

1 Introduction

So far, the characteristic of the GIS non X-ray background (hereafter NXB) were reported by H. Kubo et al. (ASCA News No. 2) and by Y. Ikebe et al. (ASCA News No. 3). In this article, we report more detailed properties of the GIS NXB, particularly about its time variation, and discuss reproducibility of the GIS NXB with several methods of NXB estimation. Methods developped here was actually utilized for the Cosmic X-ray background (hereafter CXB) analyses (Y. Ishisaki 1996; Y. Ueda 1996). See also K. Makishima et al. (1996), which contains some part of this article as well as most of previous two.

We utilized the night-earth data, i.e., events obtained when the XRT was pointing to the night-side of the Earth, following the previous NXB studies. Because there are some contamination of solar X-rays when the day-side of the Earth are partially visible from the satellite, even when it is outside of the GIS f.o.v., we further set a condition that sun height from the rim of the Earth $\leq -5^\circ$ (the Sun locates behind the Earth). Results shown in this article are based on the night-earth observations from June 1993 to June 1995, which amount to 1,400 ks (figure 1, 2). In figure 2, we find a long-term NXB increase by $\sim 15\%$ in two years, which is probably caused by a gradual build-up of long-term decay radioisotopes.

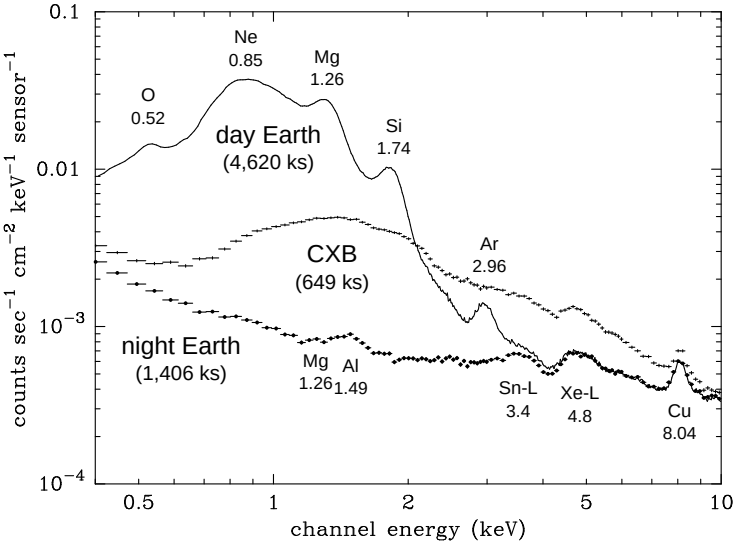

Figure 1: Integrated spectra of the day-earth (smooth line), the CXB (crosses), and the night-earth (filled circles) observations taken by the GIS2+3 on the whole detector area ($r \leq 25$ mm without ^{55}Fe calibration isotope). Each of the exposure time is given in the parentheses. The CXB and the day-earth spectra contains NXB. Possible origin of the line feature with the energy in keV are also given in the figure. The flare-cut (table 1) is NOT applied.

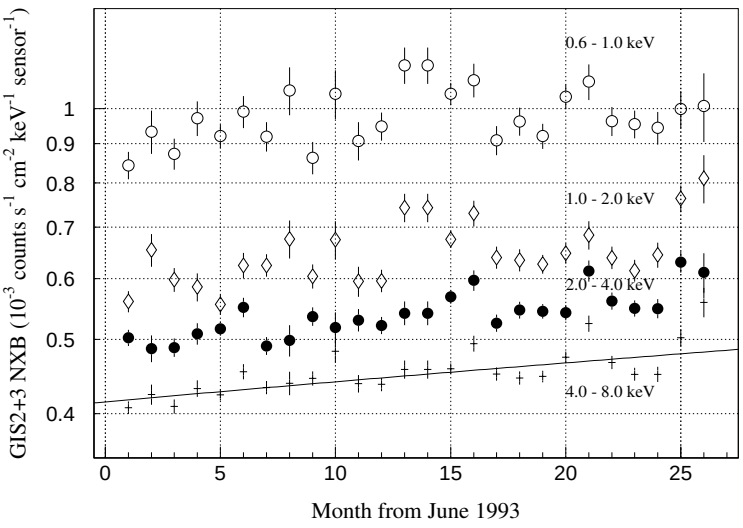

Figure 2: Long term (June 1993–June 1995) variations of the GIS2+GIS3 counting rate during the night-earth observations in the 0.6–1.0 (open circle), 1.0–2.0 (diamond), 2.0–4.0 (filled circle), and 4.0–8.0 (crosses) keV energy bands, integrated within the radius of 20 mm from the optical axis, where x-axis is time in unit of months. A solid line on the data of 4.0–8.0 keV band shows the best fit line of $y = 0.00257x + 0.414$. The flare-cut (table 1) is applied.

2 Flare-events and the GIS monitor counts

As reported previously in the ASCA News No. 2 and 3, time variation of the GIS NXB is predominantly correlated with geomagnetic cut-off rigidity (hereafter ***COR***) for cosmic rays along the satellite orbit. Although COR is a good indicator of NXB, COR is merely one of many factors that affect NXB. Therefore, we utilized the GIS monitor counts to estimate NXB. Among nine GIS monitor count items (ref. T. Ohashi et al. 1996), we selected $H0$ (too large pulse-height and too short rise-time) and $H2$ (too large pulse-height and too large rise-time) as the NXB indicator, because they are almost free from signal X-rays in the f.o.v., even during the on-source observations. $H0$ and $H2$ have adequate statistics of 10–30 c s^{-1} $sensor^{-1}$ when they are summed up. Since GIS2 and GIS3 show similar variations, we still sum the counts of GIS2 and GIS3. Hereafter, we call this summed up counts "***H02***". Figure 3 shows a correlation between COR and $H02$, which has almost the same distribution as COR vs. $LDHIT$. As shown in figure 5, $H02$ and COR also correlate well to the night-earth data counts inside 17 mm radius (hereafter ***NTE***). However, there are several issues on these correlations.

The first problem is a secondary branch below $COR \sim 10$ GeV c^{-1} on the COR correlation, as shown in figure 3. This is due probably to a slight inaccuracy of our COR-map. If we plot the satellite positions on the Earth, those periods which fall on the secondary branch appear only at the north east region of the map above the north Atlantic Ocean (dots in figure 4). Since the COR-map which we use does not refer to the satellite height, this discrepancy may change in future when the satellite altitude decreases.

The next problem is a large scatter around $COR \sim 11$–12 GeV c^{-1} in the COR vs. $H02$ plot, which is also seen in COR vs. NTE (figure 5b). We call this phenomanon "**hard-flares**". If we plot the satellite positions on the Earth, the hard-flare periods are concentrated in the region peripheral to the south Atlantic anomaly (SAA; filled circles in figure 4). The hard-flares are probably caused by particles trapped in SAA. These events can be eliminated by rejecting time intervals when $H02 > 1.5 \times f(COR)$ in figure 3.

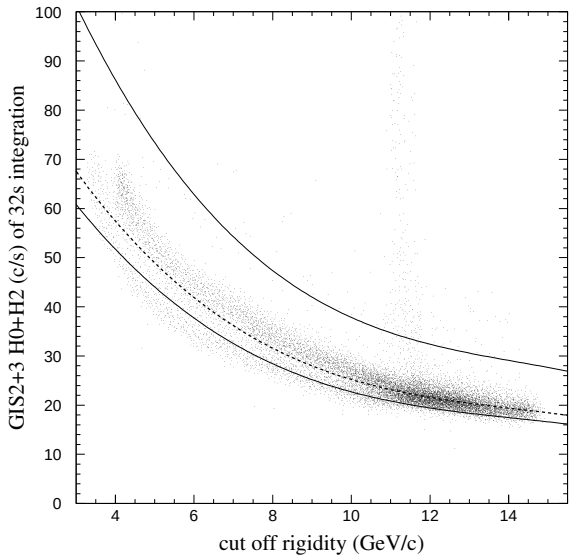

Figure 3: Correlation between COR and $H02$ counts during the night-earth observations, where x-axis is COR in GeV c^{-1}. $H02$ is integrated for every 32 s. A dashed line means a function $f(x) = (109.3 - 17.05x + 1.127x^2 - 0.02627x^3)/32$ derived from fitting. Two solid lines below and above show $f(x)$ scaled by 0.9 and 1.5 times, respectively. The flare-cut (table 1) is NOT applied.

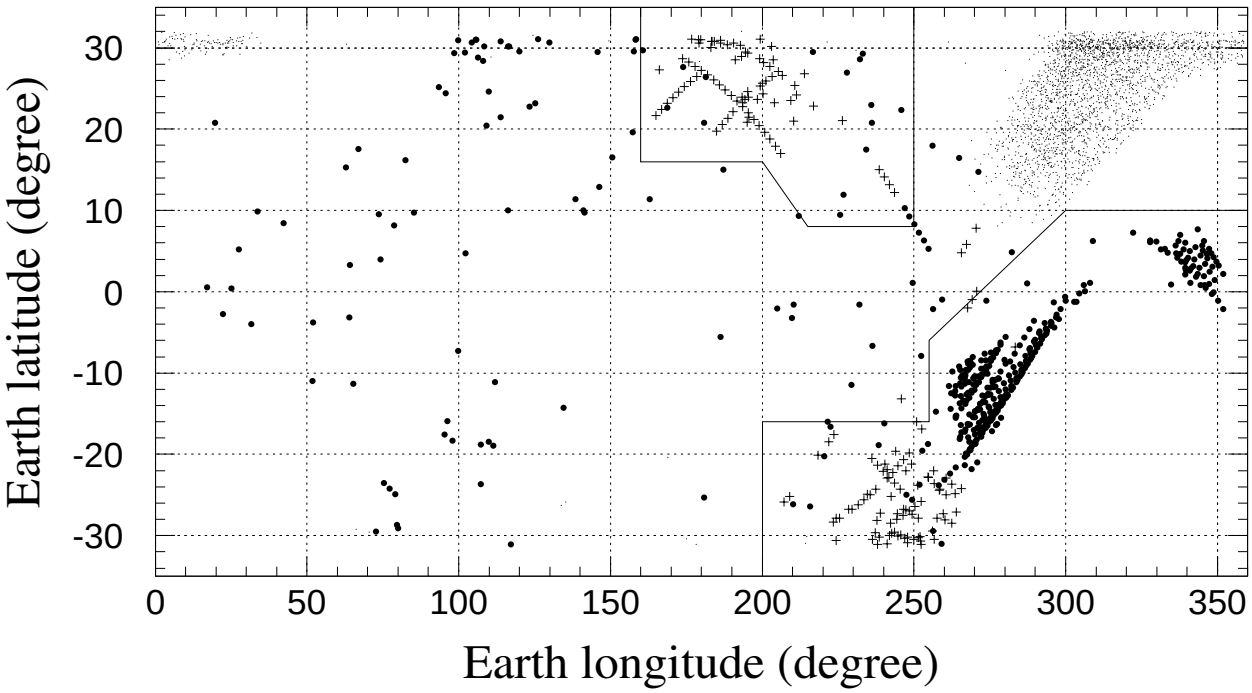

Figure 4: Distribution map for three types of phenomena on the Earth surface. The mark "$\cdot$" represents a position when $H02$ is less than the lower solid line in figure 3, where the COR-map is thought to be inaccurate. The mark "$\bullet$" represents a position when $H02$ is greater than the upper solid line in figure 3 (the hard-flares). The mark "+" represents a position when $H02 < 1000$ c/32 s $= 31.25$ c/s and $NTE > 15$ c/32 s $= 0.46875$ c/s in figure 5a (the soft-flares). Two regions surrounded by solid lines define the dangerous areas where we should be cautious of the hard- and the soft-flares.

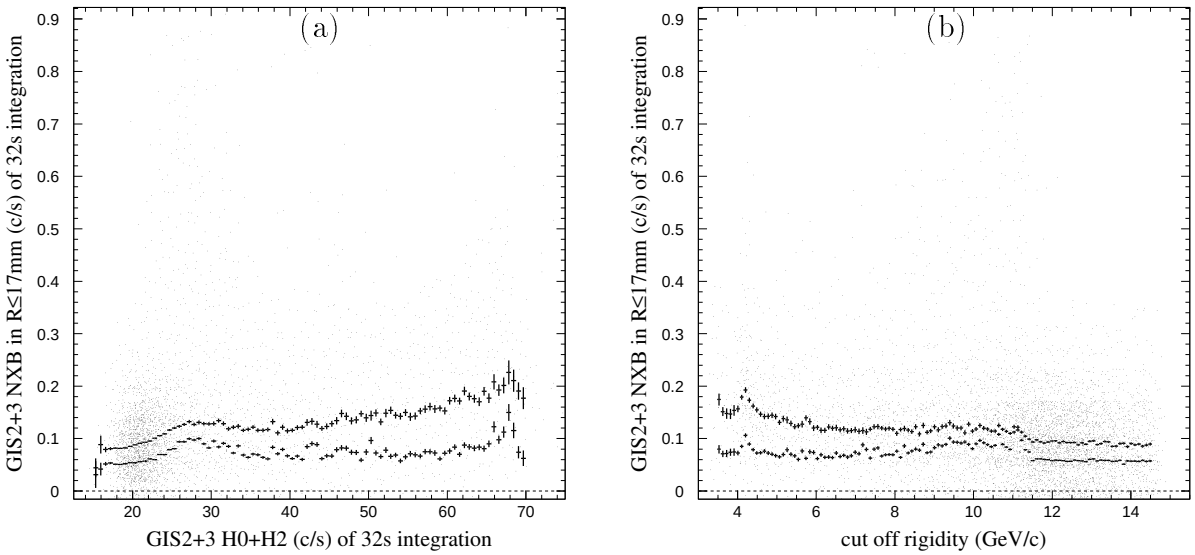

Figure 5: (a) A correlation between $H02$ and NTE, and (b) a correlation between COR and NTE. $H02$ and NTE are integrated for every 32 s. NTE is integrated in $r \leq 17$ mm in the 0.3–11 keV energy band. Crosses superposed on the figure show averages (upper) and standard deviations (lower) in each $H02$ or COR bins. The flare-cut (table 1) is NOT applied.

After eliminating the hard-flares, we encounter yet another issue, i.e., the component which scatters upwards around $H02 \sim 20$–40 in figure 5a. We call this phenomenon "**soft-flares**". During the soft-flares, the NXB counts increase without an increase of $H02$. We need more caution for the soft-flares than the hard-flares, because they cause mis-estimation of the NXB counts, and furthermore, the spectrum during the soft-flares show acutually harder profile than the average spectrum for the entire night-earth observations. If we plot the satellite positions on the Earth, the soft-flare periods are concentrated in two regions: the south west to SAA and above Hawaii (crosses in figure 4). Although the soft-flares could be eliminated by masking these regions, the associated loss in exposure would be too large. We found that $RBMCNT$, i.e., a counting rate of the radiation belt monitor (RBM; ref. T. Ohashi et al. 1996), can reject the soft-flares efficiently. As shown in figure 6, $RBMCNT$ distribution during the soft-flares (thick line) is almost flat, in contrast to the distribution for the entire night-earth observations (thin line) which is concentrating towards $RBMCNT < 25$ c/s. Therefore we reject the time intervals when $RBMCNT > 300$ c/16 s = 18.75 c/s everywhere, and especially $RBMCNT > 100$ c/16 s = 6.25 c/s in the dangerous areas (solid line in figure 4). We add the $RBMCNT$ distribution map on the Earth in the appendix of this article for reference.

The frequency of the soft-flares have a slight correlation with the angle θ_{mag} of the terrestrial magnetic field to the XRT direction. The soft-flares seem to happen more frequently when $\theta_{mag} \sim 60$–120°. It is possible that the physical origin of the soft-flares is electrons which come into the GIS from the direction of the XRT.

From these investigations, we have arrived at the conditions to reject the hard- and soft-flares as summarized in table 1. To avoid high NXB periods, we usually restrict $H02$ in the range of 15–45 c/s, too. We call the procedure to apply these conditions "**flare-cut**". Correlations between $H02$ vs. NTE and between COR vs. NTE after the full flare-cut are shown in figure 7.

Table 1: Summary of the flare-cut conditions

Condition	Reason
15 c/s $\leq H02 \leq$ 45 c/s	to avoid high NXB
$H02 \leq 1.5 \times f(COR)^{\dagger}$ c/s	for hard-flares
$RBMCNT \leq$ 300 c/16 s = 18.75 c/s everywhere	for soft-flares
$RBMCNT \leq$ 100 c/16 s = 6.25 c/s in the dangerous areas (figure 4)	for soft-flares

† $f(x) = 0.5(109.3 - 17.05x + 1.127x^2 - 0.02627x^3)$ c/ 16 s.

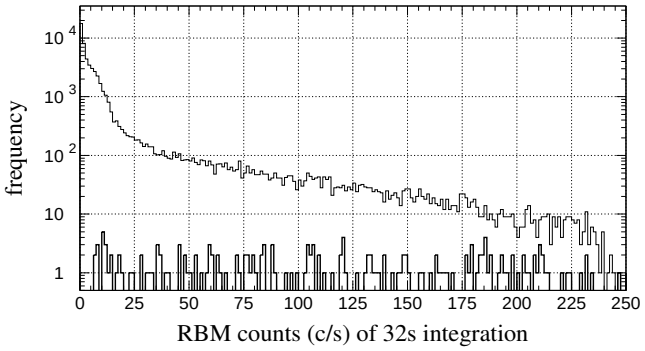

Figure 6: $RBMCNT$ distribution for the entire night-earth observations (thin solid line) and during the soft-flares (thick line).

Compared with figure 5, the humps around $H02 \sim$ 20–40 and $COR \sim$ 10–12 have almost disappeared. The standard deviation of NTE in each bin are approximately equal to the square root of the average NTE of that bin, which means the Poisson statistics. This means that the NXB counts can be successfully estimated by $H02$.

3 NXB reproducibility in the GIS

When analyzing the GIS data, either spectrally or spatially, we usually subtract background derived from blank-sky observations. In such cases, the background reproducibility is limited by two factors; the field-to-field fluctuation in the CXB brightness, and the NXB variation. In fact, the NXB count rate can vary by $\sim 40\%$ in the range of $COR > 6$ GeV c^{-1} (figure 7). If the exposure time is long, e.g. 100 ks, this variation is averaged to a reasonable level of $\sim 10\%$ (table 2) depending on the length of the observation. But it will be better to take into account the NXB variation by some methods. As seen in the previous section, $H02$ can be a good indicator of NXB. Thus we choose $H02$ to predict the NXB variation. Below, we explain how to generate the expected NXB spectrum for a specified on-source observation.

We sort the night-earth data according to the level of $H02$ counts estimated in every 16 seconds. Figure 8 shows the night-earth spectra and radial profiles corresponding to five $H02$ intervals. As $H02$ increases, the spectrum gets softer and the slope of the radial profile gets steeper towards the detector rim. It is due probably to the increase of the *soft-component* of NXB

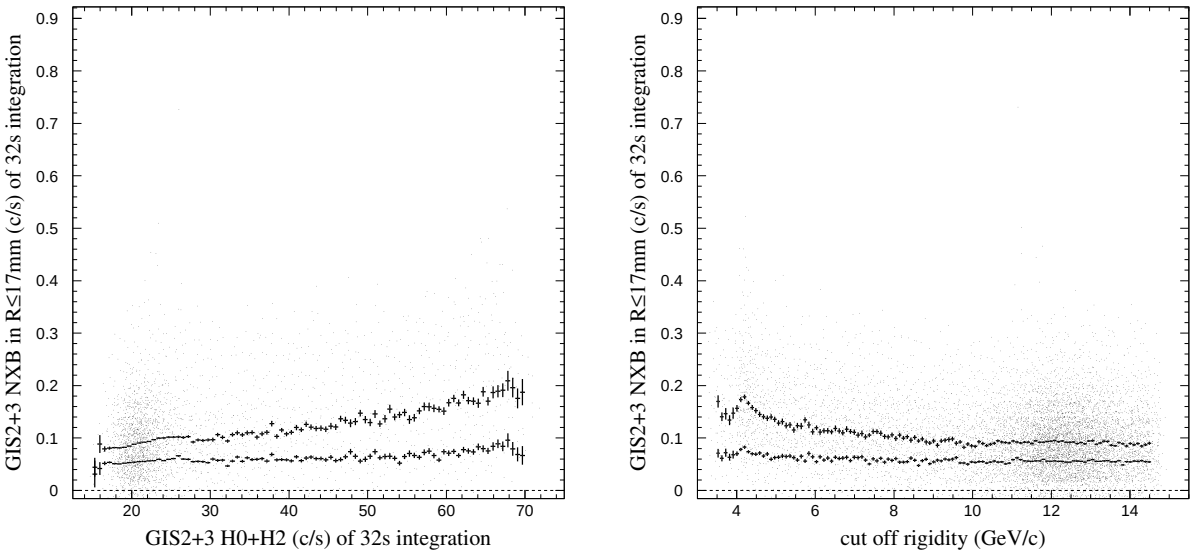

Figure 7: Almost the same as figure 5 except that the flare-cut (table 1) is applied.

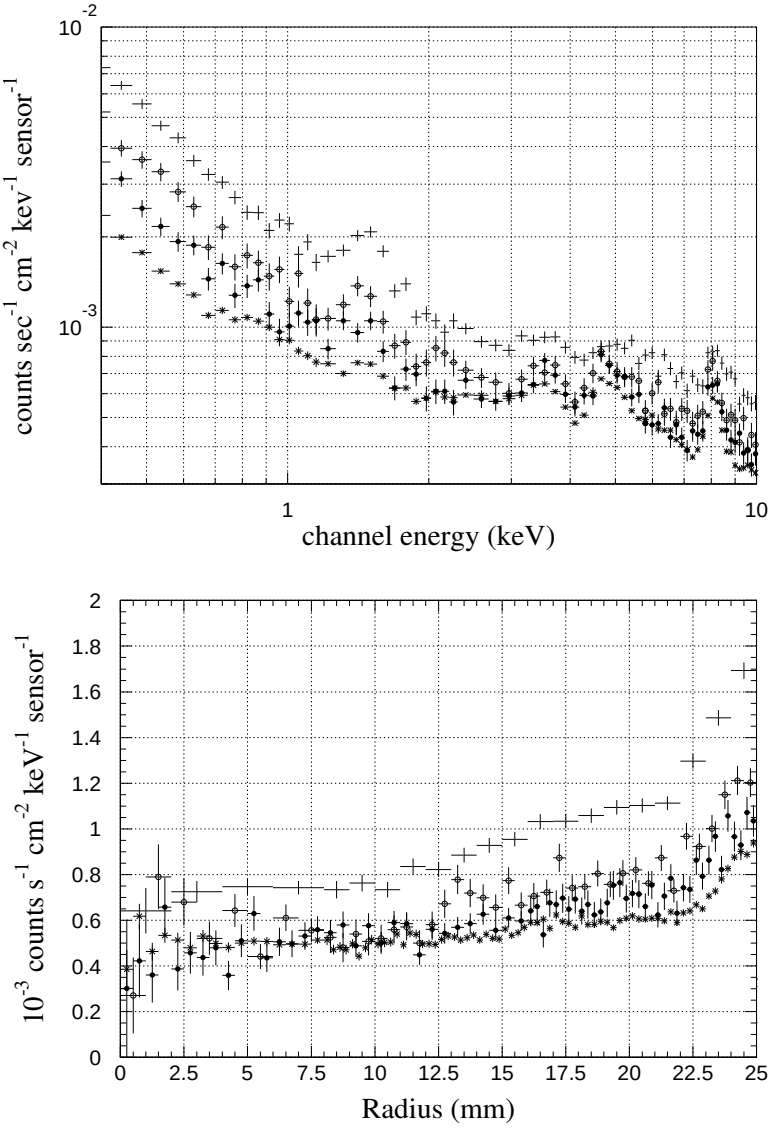

Figure 8: $H02$ sorted spectra (upper panel) and radial profiles (lower panel) of the GIS counts during the night-earth observations in the 0.6–7.0 keV energy band. The mark '+' represents the data when $H02$ is in the range 50–80 c/s, '○' 40–45 c/s, '●' 30–35 c/s, and '×' 20–25 c/s. $H02$ are integrated for every 16 s. The flare-cut (table 1) is applied.

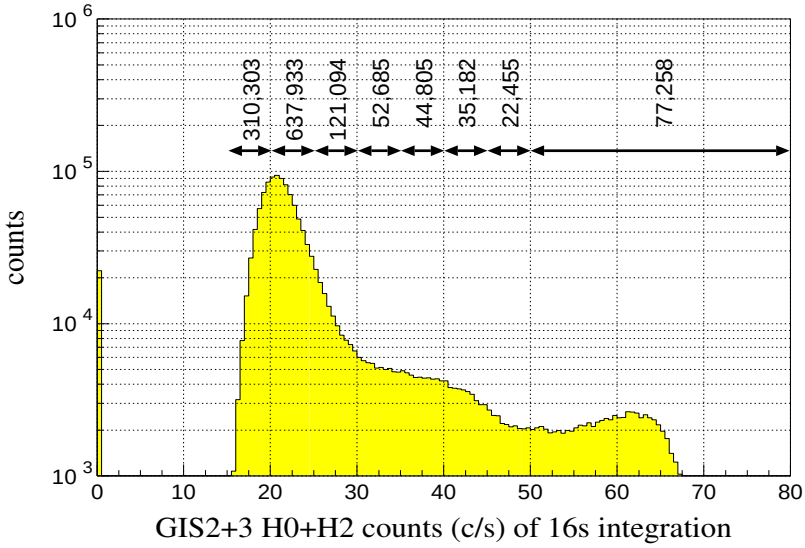

Figure 9: $H02$ distribution for the entire night-earth observations. Net exposure time (sec) in each 5 c/s bin of $H02$ is given in the figure. The flare-cut (table 1) is applied.

described in H. Kubo et al. (ASCA News No. 2). We usually restrict $H02$ to the range of 15–45 c/s, where the influence of the *soft-component* is not severe. Figure 9 shows distribution of exposure time out of the entire night-earth observations, sorted as a function of $H02$. We denote each exposure time T_i^{NTE}, and each spectrum $H_i^{NTE}(PI)$, both of which are counted or created on the same condition and in the same detector region as the on-source observations. When T_i^{OBS} is the exposure time in the i-th $H02$ bin during the on-source observation, the NXB spectrum contained in the on-source data is estimated as:

$$H(PI) = \sum_i H_i^{NTE}(PI)\ \frac{T_i^{OBS}}{T_i^{NTE}}. \qquad (1)$$

We call this method "**H02-sorting method**".

To check the reproducibility of NXB by the H02-sorting method, we splitted the entire night-earth data into 122×10 ks intervals. Then we compared the counting rate of each interval with that estimated by H02-sorting method using the entire night-earth data. The results are shown in figure 10. Crosses in the upper panel show the actual counting rate of each interval, and the histogram show the prediction. It seems that 10 ks-integrated NTE varies more than the prediction. There is a general trend of increasing counting rate with time, which means that the long-term NXB increase which is seen in figure 2 cannot be reproduced by the H02-sorting mothod. As seen in the lower panel of figure 10, the mean value of observed / predicted ratio is 0.9983 and very close to 1.0, which is rather natural because their mother groups are the same. The standard deviation of the distribution is 0.07429, which mean 7.4% rms variation of the NXB counts. This value includes a Poission error of 3.4%; therefore, systematic error of the H02-sorting method for 10 ks observation is thought to be 6.7%. If we use the average NTE instead of the H02-sorting method prediction, the systematic error increases to 7.8%. Thus the H02-sorting method reduces the systematic errors by about 1% level. Since the χ^2/d.o.f of the line fitted to the ratio shown in middle panel is $412.4/121 = 3.4$, the systematic error will be reduced to $\sqrt{3.4 - 1.0} \times 3.4\% = 5.2\%$, if the prediction of H02-sorting method are corrected for the long-term trend.

This long-term NXB increase of $\sim 15\%$ in two years can be a serious problem for a faint source

Table 2: Average count rate and reproducibility of the 0.7–7 keV NXB

data screening condition	NXB subtraction method	0.7–7 keV† counting rate (c s^{-1} cm^{-2} keV^{-1})	live‡ time fraction	rms estimation error 10 ks	40 ks
$COR \geq 6$ GeV c^{-1}	average NTE	4.01×10^{-4}	92%	16%	14%
flare-cut	average NTE	3.59×10^{-4}	74%	7.8%	5.6%
flare-cut	H02-sorting method	3.59×10^{-4}	74%	6.7%	5.3%
flare-cut	+ long-term correction	3.59×10^{-4}	74%	5.3%	3.4%

† Average NTE in the 0.7–7 keV energy band within the radius of 20 mm from the optical axis
‡ Reduction rate of exposure time to the entire night-earth observations

analysis as well as for an extended source analysis (extreme case is the CXB). No compensation of this long-term trend results in a NXB under-subtraction for recent observations especially in harder energy bands, which may cause an artificial hard tail. In fact, it can make ~ 0.1 difference of the CXB photon indices between two observations at intervals of two years. We, therefore, adjustted the normalization of the NXB image or spectrum estimated by the H02-sorting method with a formula:

$$scaling\ factor = 0.9983 + 2.1255 \times 10^{-9} \cdot (ascatime - 45878400), \quad (2)$$

where $ascatime$ represents the time in second from 00:00:00 (UT) on 1 January 1993, and is calculated from the mean observation time.

The systematic errors described above are summarized in table 2. We conclude that we can achieve a $\sim 3.5\%$ rms reproducibility in regard to NXB count rate, by a combined use of the standard background rejection, the flare-cut procedure, the H02-sorting method, and the long-term NXB trend correction.

4 Summary

The night-earth data from June 1993 to June 1995 shows a long-term NXB increase by $\sim 15\%$. We found NXB correlates well with $H02$, if hard- and soft-flares are carefully excluded. We can estimate the NXB counts with $\sim 15\%$ error, when naive NXB rejection of $COR \geq 6$ GeV c^{-1} and an estimate by averaging night-earth data are applied. We can achieve 3.5% reproducibility at best with flare-cut, H02-sorting, and long-term trend correction.

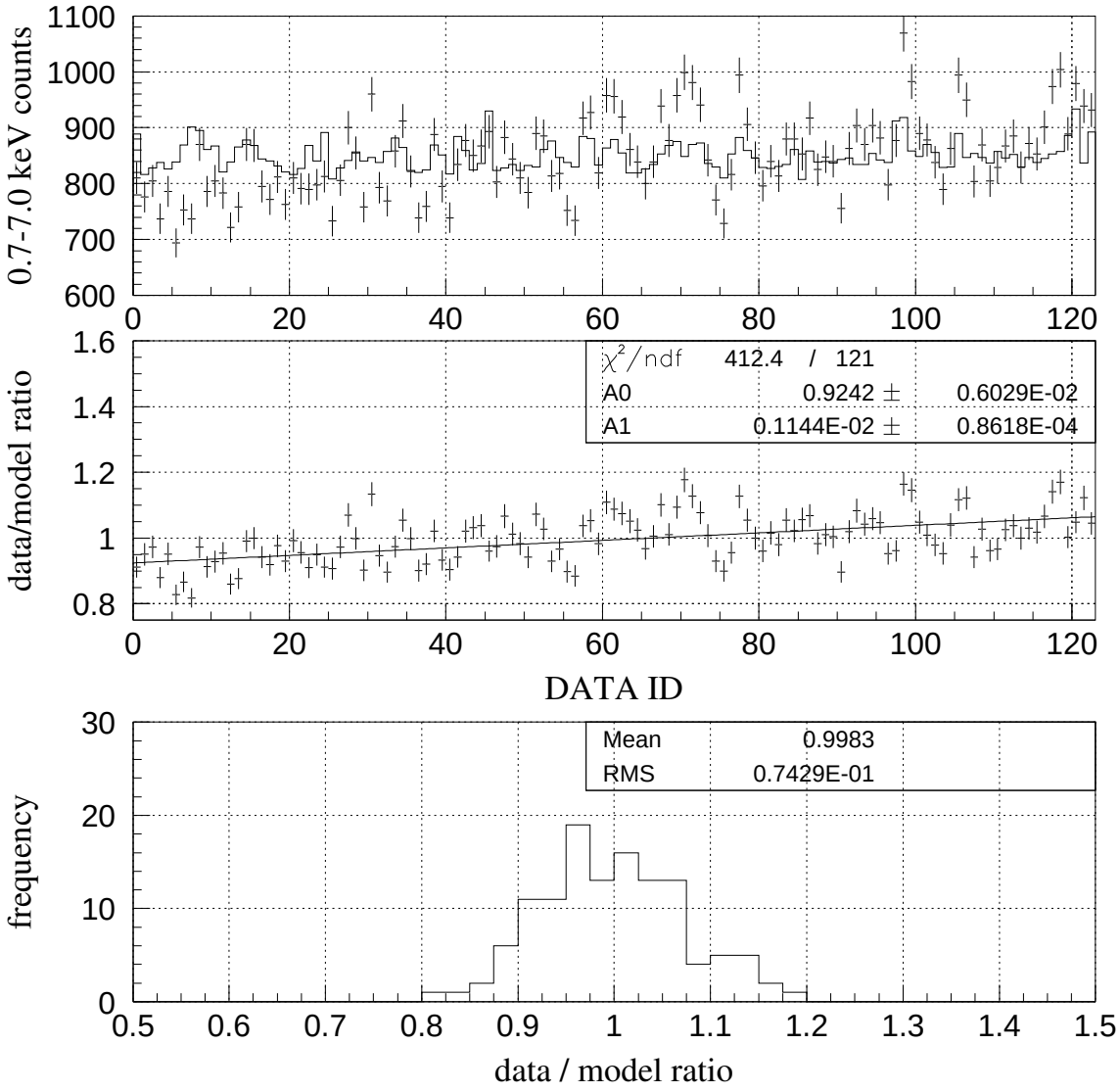

Figure 10: Figures to check the NXB reproducibility by H02-sorting method. Upper panel shows the actual NTE (crosses) and the H02-sorting method prediction (solid line), in the 0.7–7.0 keV energy band, for every 10 ks exposure. Middle panel shows ratios of the NTE to the prediction. The solid line shows the best fit line, and fitting results are indicated in the figure inset. Lower panel shows a distribution of the ratios. The mean value and the standard deviation for the distribution are indicated in the figure.

References

Kubo, H. et al., 1994, ASCA News No. 2, p14
Ikebe, Y. et al., 1995, ASCA News No. 3, p13
Ishisaki, Y. et al., 1995, ASCA News No. 3, p19
Ishisaki, Y., 1996, PhD thesis, the University of Tokyo
Ueda, Y., 1996, PhD thesis, the University of Tokyo
Ohashi, T. et al., 1996, *Publ. Astron. Soc. Japan* **48**, 157–170
Makishima, K. et al., 1996, *Publ. Astron. Soc. Japan* **48**, 171–189

Appendix. RBM count distribution map

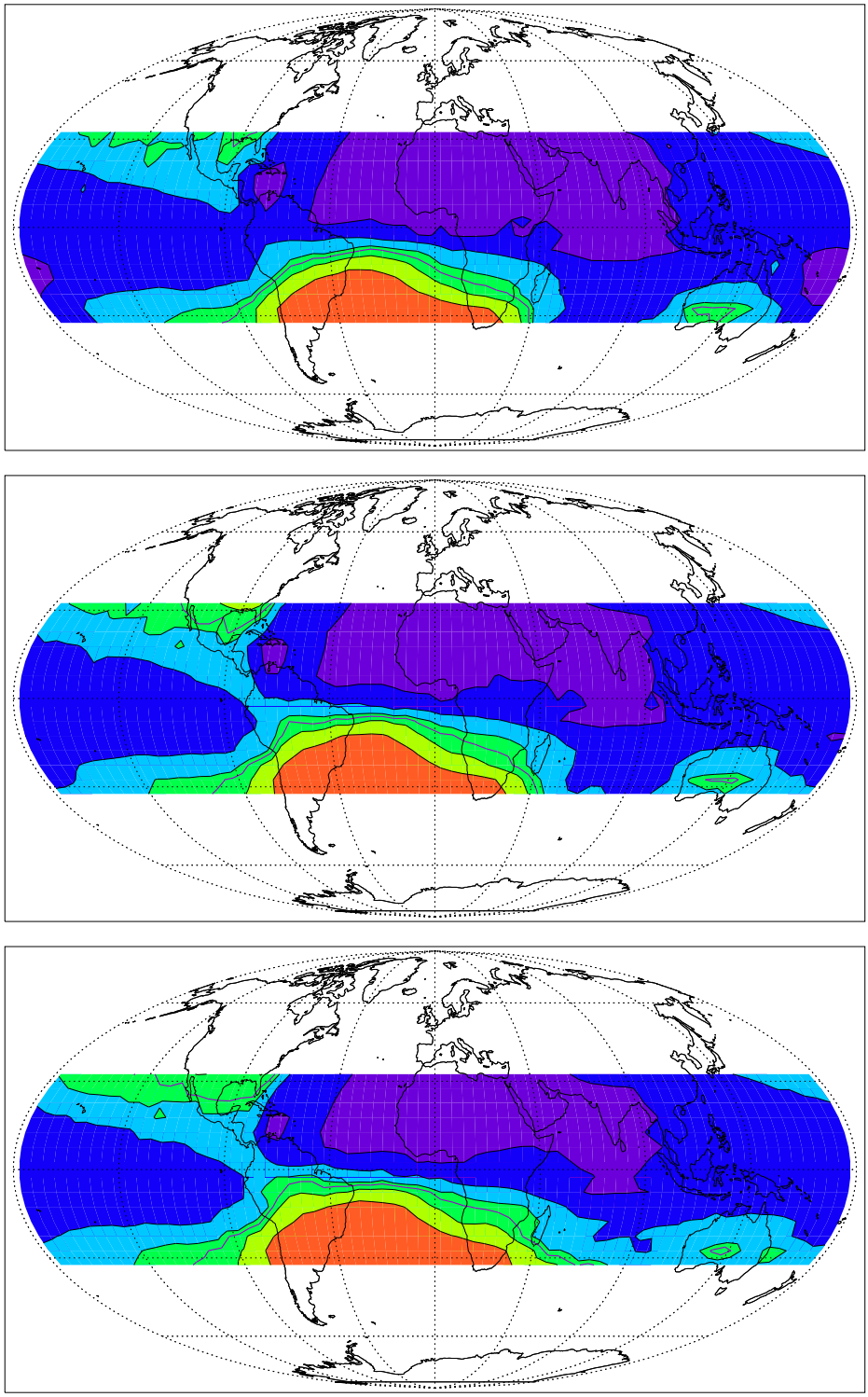

Figure 11: RBM count distribution map on the Earth (May–November 1993) sorted by the satellite altitude; TOP: 520–550 km, MID: 550-600 km, BOTTOM: 600–630 km. The contour step is every one magnitude, as purple < 1 c s^{-1} and orange > 10000 c s^{-1}, with the red line showing where RBM-flag is set (256 c s^{-1}). This figure is supplied by T. Mihara (RIKEN), and color figures can be obtained from http://crow.riken.go.jp/~mihara/reports/RBMreport/.